JGR Solid Earth

RESEARCH ARTICLE
10.1029/2025JB031994

Reactivation of Pre-Existing Rifted Basin by Forced Subduction Initiation in the South China Sea

Fan Zhou[1,2], Jie Liao[1], and Laetitia Le Pourhiet[3]

[1]School of Earth Sciences and Engineering, Sun Yat-sen University, and Southern Marine Science and Engineering Guangdong Laboratory (Zhuhai), Zhuhai, China, [2]Laboratoire de Géologie Département de Géosciences, CNRS UMR 8538, École Normale Supérieure, PSL University, Paris, France, [3]Sorbonne Université, CNRS-INSU, Institut des Sciences de la Terre Paris, ISTeP UMR 7193, Paris, France

Key Points:

- 2D geodynamic models are built to study the anomalous tectonic subsidence in the Pearl River Mouth Basin adjacent to Manila Subduction Zone
- Inherited boudinage structure of the basin controls the area and rate of tectonic subsidence, central part of the basin always subsidies
- The timespan of subsidence in the basin is consistent with initiation time of subduction, linking the tectonic subsidence with subduction

Supporting Information:

Supporting Information may be found in the online version of this article.

Correspondence to:

J. Liao,
liaojie5@mail.sysu.edu.cn

Citation:

Zhou, F., Liao, J., & Le Pourhiet, L. (2025). Reactivation of pre-existing rifted basin by forced subduction initiation in the South China Sea. *Journal of Geophysical Research: Solid Earth*, *130*, e2025JB031994. https://doi.org/10.1029/2025JB031994

Received 21 MAY 2025
Accepted 4 DEC 2025

Author Contributions:

Conceptualization: Fan Zhou, Jie Liao, Laetitia Le Pourhiet
Data curation: Fan Zhou
Formal analysis: Fan Zhou, Jie Liao, Laetitia Le Pourhiet
Funding acquisition: Jie Liao
Investigation: Fan Zhou, Jie Liao, Laetitia Le Pourhiet
Methodology: Fan Zhou, Jie Liao, Laetitia Le Pourhiet
Project administration: Jie Liao
Resources: Jie Liao
Software: Jie Liao
Supervision: Jie Liao, Laetitia Le Pourhiet
Validation: Fan Zhou, Jie Liao, Laetitia Le Pourhiet
Visualization: Fan Zhou, Laetitia Le Pourhiet
Writing – original draft: Fan Zhou, Jie Liao
Writing – review & editing: Fan Zhou, Laetitia Le Pourhiet

Abstract Basin inversion, involving the transition from extensional to compressional stress, has been extensively studied. Traditional theories predict uplift and erosion of extensional basin structures during inversion, yet some rifted basins, like the Pannonian Basin in southeastern Central Europe and the Pearl River Mouth Basin (PRMB) in the Northern South China Sea (SCS) show sustained subsidence even under compression. Previous sandbox experiments and numerical models mostly focus on fault inversion at the scale of sedimentary basins and overlook large-scale boundary conditions, such as compression from subduction initiation. Here, we investigate the anomalous subsidence in the PRMB, adjacent to the SCS and the Manila Subduction Zone. Using two-dimensional numerical models and varying basin wavelength and thickness, and the convergence velocity of the upper plate to explore how rifted basin responses to the subduction. Our results show that subduction initiation can sustain central basin subsidence for >1 Myr, with high tectonic subsidence rates (>0.4 mm/yr) despite compression. The lithosphere undergoes both lithospheric- and crustal-scale buckling; the latter dominates when inherited structure has short wavelength, enhancing distributed deformation and broadening the subsiding area. Basin subsidence exhibits a periodic feature, including a "reactivation stage" with high tectonic subsidence rate triggered by subduction initiation. The inherited boudinage structure promotes distributed deformation and tectonic subsidence, while subduction velocity enhances the overall subsidence rate. The characteristic wavelength of deformation depends primarily on inherited structure and lateral variations in lithospheric strength. Overall, our results emphasize the importance of subduction induced compression and the inherited structure on basin inversion.

Plain Language Summary The Pearl River Mouth Basin began accumulating sediments in grabens, topographic depressions formed by downward movement along normal faults, approximately 80 to 65 million years ago. This occurred as a result of distributed crustal extension, which ultimately led to the opening of the South China Sea around 32 million years ago. When the nearby Manila Subduction Zone initiated 20 million years ago due to compressional forces, geologists typically expected the graben faults to be reactivated in reverse, leading to uplift and erosion of the sedimentary rocks. Instead, sediment accumulation accelerated locally, accompanied by unexpected subsidence in the basin. Our study uses computer models to investigate this unexpected subsidence. The results reveal that inherited variations in crustal thickness and wavelength, known as boudinage, play a significant role in controlling how the basin responds to tectonic forces, helping to explain the observed patterns of continued subsidence.

1. Introduction

Glennie et al. (1981) were the first to use the term "inversion" to describe the transition of extensional basins into compressional regimes, primarily based on field observations in sedimentary basins. This term now refers to basins or grabens in different tectonic settings that undergo a transition from an extensional to a compressional stress regime, where compression is typically driven by a tectonic event, such as subduction (Cooper et al., 1989), and has been widely recognized in basins around the world over a long period (e.g., Baranov et al., 2002; Frimmel & Fölling, 2004; Fyhn et al., 2010; Horváth & Cloetingh, 1996; Rosa et al., 2023; Sun et al., 2014; Suo et al., 2020; Wang et al., 2017; Ziegler, 1987). Subsequent studies further classified basin inversion processes into: (a) observational studies documenting structural and stratigraphic evidence (e.g., Cooper et al., 1989; Turner & Williams, 2004), (b) numerical models simulating lithospheric flexure and stress evolution (Cloetingh & Burov, 2011; Rosa et al., 2023; Schmalholz & Podladchikov, 1999), and (c) analog experiments investigating

fault reactivation patterns (Del Ventisette et al., 2006; Wang et al., 2017). The inversion process is now recognized to involve multiple phases: (a) fault reactivation and uplift, marked by reverse faulting and erosion (Fyhn et al., 2010; Turner & Williams, 2004); (b) potential continued subsidence in some basins due to lithospheric weakening or distributed deformation (e.g., Perron et al., 2021; Suo et al., 2020). While reverse faulting is typically associated with basin uplift during inversion (Turner & Williams, 2004), some cases, including the Pannonian Basin in southeastern Central Europe and Xihu Sag in Eastern China, exhibit concurrent subsidence despite compression—a paradox attributed to regional stress distribution due to locked stable continental environment or oblique stress partitioning due to fault geometry (Horváth & Cloetingh, 1996; Wang et al., 2017).

To investigate the mechanisms and factors influencing the evolution of basin inversion, sandbox experiments have been widely used (e.g., Bonini et al., 2012; Buchanan & McClay, 1991; Granado et al., 2017; Keller & McClay, 1995; Marques & Nogueira, 2008; Pinto et al., 2010; Schöfis et al., 2022). However, the fixed lower boundary used in these sandbox experiments limits mantle convection beneath it, and most of them focus on basin structure without accounting for the regional tectonic setting at larger scales, such as subduction zones. Numerical simulations have also been employed to study basin inversion (e.g., Buiter et al., 2009; Dai et al., 2014; Jourdon et al., 2019; Lafosse et al., 2016; Li et al., 2021; Oravecz et al., 2024; Yang et al., 2016), allowing for the inclusion of thermal effects and isostatic responses but they primarily focus on the rifted basin itself under changing boundary conditions, often neglecting the influence of external forcing such as subduction, and without correcting for boundary condition effects.

The South China Sea (SCS) lies between the Pearl River Mouth Basin (PRMB) and the Manila Subduction Zone (MSZ) (Figure 1a), the latter acting as the source of compressional stress during basin inversion since its initiation (Li et al., 2021). The mechanism of subduction initiation (SI) can be either induced or spontaneous (Stern, 2004; Stern & Gerya, 2018; Zhou et al., 2018). The former one requires an external driving force, such as the pull of a subducted slab or compression from a mid-ocean ridge (Arculus et al., 2015), whereas the latter one occurs along fault zones or weak zones due to the density difference between the subducting plate and the uplifted half-plate (Gerya, 2011; Gurnis et al., 2004; Stern & Gerya, 2018). In the case of the Manila Subduction, it is induced by westward motion of the Philippine Sea Plate (PSP) above the SCS, when subduction occurs, the SCS plate experiences tectonic compression from Manila Subduction and transfers this compression to the PRMB (Wu et al., 2016). Previous models simplified the influence of the Manila Subduction as an "accordion"-type boundary condition and neglected the inherited boudinage structure of the PRMB (Li et al., 2021). This study focus instead on the influence of subduction-induced tectonic compression on rifted basins during inversion with inherited boudinage structure, taking the PRMB as an example. Here, we examine the anomalous subsidence observed in the PRMB using 2D numerical models to investigate the relationship between the anomalous tectonic subsidence observed in the PRMB and adjacent Manila Subduction.

In summary, the uplift and erosion of basins are commonly considered distinctive indicators of basin inversion. However, an increasing body of evidence suggests that, even in a rifted basin undergoing the transition from extension to compression, the response of the basin to the shift in stress regime can be contradictory, ranging from uplift to subsidence. This is exemplified by the observed increase in tectonic subsidence rates in the PRMB (Figure 1b). Simultaneously reproducing, the rifting of the PRMB and the SCS along with the initiation of the Manila Subduction is difficult to achieve within a single modeling without precise constraints from reconstructions. However, as products of continental rifting, the boudinage structure of rifted basins (Zhou et al., 2025) can be represented and calibrated by varying crustal thickness and wavelength. In this study, our models aim to investigate the interaction between the rifted basin with inherited boudinage structure and forced subduction initiation of the Manila Subduction, using a left fixed boundary representing the strong South China block (SCB) and a right converging upper plate representing the PSP.

2. Tectonic Setting and Structure of the Pearl River Mouth Basin (PRMB)

The PRMB (Pearl River Mouth Basin) formed during Mesozoic-Cenozoic and is located in the northern part of the SCS (Figure 1a), with >30 Myr rifting history since >65 Ma to ~34 Ma (Figures 1c and Pinglu & Chuntao, 1994). The continental margin experienced NW-SE and N-S extensions during rifting and E-W compression in the post-rift stage (Franke et al., 2014; Hutchison, 2004; Sun et al., 2019). Drilling data reveal a well-preserved stratigraphic succession in the PRMB (Pang et al., 2007), showing a progressive evolution from the Wenchang Formation (Middle Eocene) at the base, through the Enping (Late Eocene–Early Oligocene), Zhuhai (Late

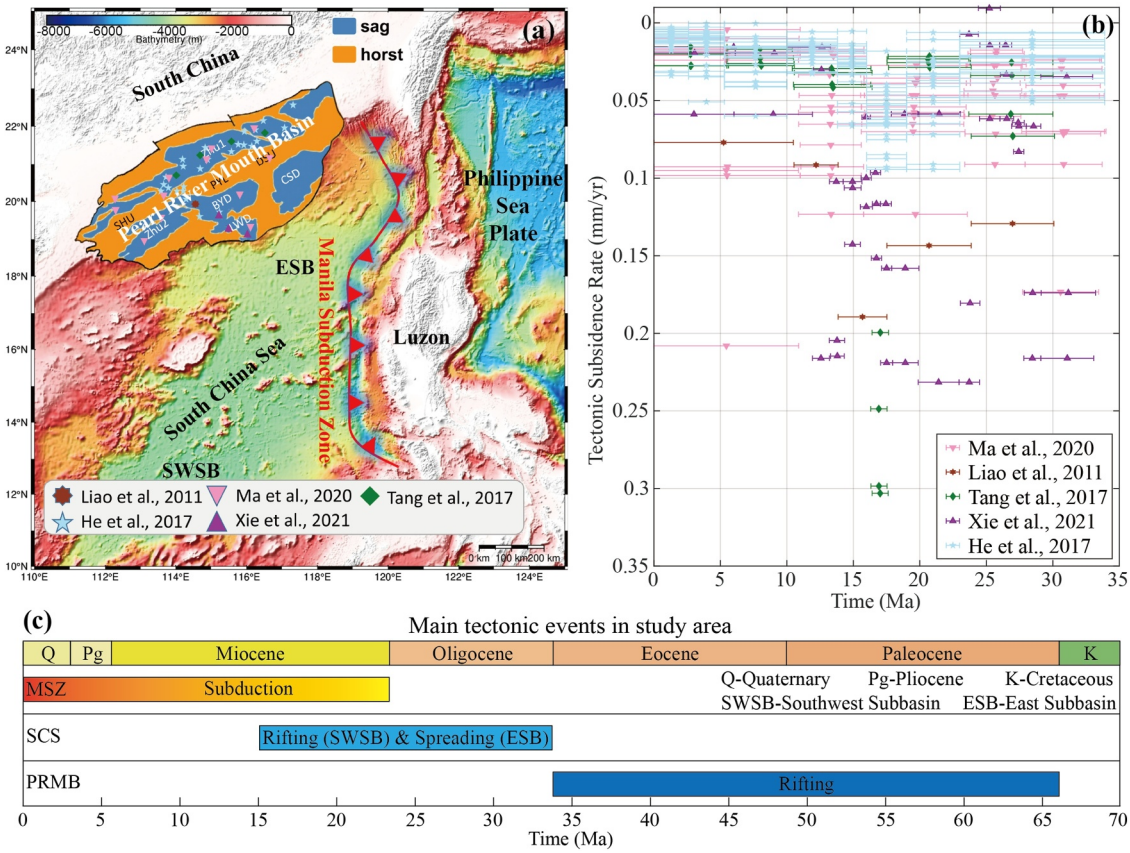

Figure 1. Tectonic setting surrounding the PRMB, with tectonic subsidence rate in the PRMB and main tectonic events in this area. (a) Tectonic setting surrounding the PRMB. Zhu1, Zhu2, BYD, CSD, LWD are names of depressions, SHU-Shenhu Uplift, PYL-Panyu Low uplift, DSU-Dongsha Uplift. (b) The tectonic subsidence rate of different parts of the PRMB since 33.5 Ma, see positions of wells in (a). (c) Main tectonic events in study area since Cretaceous, modified from Sun et al. (2014). MS-Molucca Sea, MSZ-Manila Subduction Zone, PSCS-Proto South China Sea, PSP-Philippine Sea Plate, SCS-South China Sea, SWSB-Southwest Subbasin of the SCS, ESB-East Subbasin of the SCS.

Oligocene), Zhujiang (Early Miocene), Hanjiang (Middle Miocene), and Yuehai (Late Miocene) formations, to the uppermost Wanshan Formation (Pliocene). Abundant geophysical data image the crustal-scale boudinage structure of the PRMB with a series of horsts and sags as the results of Mesozoic-Cenozoic continental rifting from the SCB (Cameselle et al., 2020; Deng et al., 2020; Zhang et al., 2023). This structure features 10s to 100 km wavelength and crustal thickness ranging from 15 to 25 km, depending on the directions of seismic lines across the PRMB, and also surrounding the SCS (Franke et al., 2014; Savva et al., 2014). In the PRMB, geophysical results also identified reverse faults related to the basin inversion in Baiyun Sag and Beibuwan Basin from west to east (Sun et al., 2014; Wang et al., 2025) since 23 Ma, this basin inversion is proposed be related to the Manila Subduction. In the western part of the PRMB, ~10 km sediments in thickness can be observed in depocenters (Li et al., 2021).

Surrounding the PRMB, there are two important tectonic units which are the East Subbasin of the SCS (ESB) and the MSZ (Figure 1a). The ESB formed as oceanic crust at ~35 Ma and ceased spreading at 15 Ma (Briais, 1993). The initiation time of the MSZ is debated, ranging from ~23 Ma (Yumul et al., 2003) to >9 Ma (Liu et al., 2020) according to different line of evidences but with more results showing 18~16 Ma. In a broader tectonic context, the PRMB formed before the opening of the ESB (~35 Ma), and prior to the initiation of the MSZ. To study the interactions between the Manila Subduction and the PRMB, we build geodynamic models that consider the continental rifting process leading to the formation of the PRMB with inherited boudinage structure. In our models, the rifted basin employs a sinusoidal geometry with varying wavelength and thickness, this geometry is reproduced by former rifting models (Li et al., 2021; Oravecz et al., 2024; Ricard & Froidevaux, 1986; Zhou et al., 2025). While geophysical observations can only show present structure, not the initial one, we vary the

crustal wavelength and thickness of the basin with corresponding lithospheric thickness according to isostacy. Besides, knowing that the SCS subducted under the PSP, with 300∼600 km shortening distance and changing front angle between them until today (Wu et al., 2016), but with arguing initiation time of the Manila Subduction from ∼23 Ma (Yumul et al., 2003) to >9 Ma (Liu et al., 2020) (corresponding to ∼3 cm/yr to ∼7 cm/yr of subducting velocity in average), the converging velocity is therefore not determined and set as a testing factor in our experiments. As the strong SCB kept almost constant position compared with the PRMB (Wu et al., 2016), a fixed left boundary is therefore set, and a leftward converging upper plate to represent the westward motion of the PSP.

3. Methods

We use the two-dimensional thermo-mechanical numerical code I2VIS (Gerya & Yuen, 2003) to study the dynamics of the basin under compression from subduction. This modeling framework based on finite-difference and marker-in-cell techniques is used to solve the mass, momentum, and energy conservation equations in a fully staggered grid. Additional modules are also employed in this study. Readers may refer to (Gerya & Yuen, 2003) for a detailed description of the employed numerical strategy.

3.1. Governing Equations

In our models, we use the governing equations to achieve the conservation of mass, momentum and energy:

$$\frac{\partial v_i}{\partial x_i} = 0$$

$$\frac{\partial \sigma'_{ij}}{\partial x_j} - \frac{\partial P}{\partial x_i} + \rho g_i = 0$$

$$\rho c_p \left(\frac{\partial T}{\partial t} + v_i \frac{\partial T}{\partial x_i} \right) = \frac{\partial}{\partial x_i} \left(k \frac{\partial T}{\partial x_i} \right) + H_r + H_s + H_a + H_L$$

where v is velocity, σ' deviatoric stress tensor, P pressure, ρ density, g gravity acceleration, c_p heat capacity, T temperature, k thermal conductivity, H_r radioactive heating rate, H_s shear heating rate ($H_s = \sigma'_{ij}\dot{\varepsilon}_{ij}$, $\dot{\varepsilon}$ strain rate tensor), H_a adiabatic heating rate ($H_a = T\alpha(\mathrm{DP}/\mathrm{DT})$, α thermal expansivity), H_L latent heating rate.

In order to achieve a free surface of the crust, a sticky air layer with a thickness of 22.5 km is implemented above the surface of the crust. The calculation of crustal sedimentation and erosion is governed by the following equation:

$$\frac{\partial y_e}{\partial t} = v_y - v_x \frac{\partial y_e}{\partial x} - v_s + v_e$$

where y_e is the vertical position of the erosion/sedimentation surface; v_x and v_y are the material velocity at the surface in x, y direction respectively; v_s and v_e are the sedimentation and erosion rates respectively, of which the values are applied by the following rules: $v_s = 0$ and $v_e = 0.315$ mm/yr when $y_e < 15$ km, $v_s = 0.315$ mm/yr and $v_e = 0$ when $y_e \geq 15$ km.

3.2. Visco-Plastic Rheology

Buckling and folding are the two fundamental deformation modes of rocks (Schmalholz & Podladchikov, 1999), they correspond to elastic and viscous deformation, respectively (Turcotte & Schubert, 2002). On a million-year scale, the flexure of the basin can be attributed to viscous deformation, which adopts a viscous deformation mechanism. In our model, the deformation calculation incorporates the viscous mechanism, which adheres to the flow laws of diffusion creep and dislocation creep. For diffusion creep, we utilize a constant critical stress (σ_{crit}) (Turcotte & Schubert, 2002), which signifies the transition stress from diffusion creep to dislocation creep.

$$\eta_{\text{diff}} = \frac{1}{2}A(\sigma_{\text{crit}})^{1-n}\exp\left(\frac{PV_a + E_a}{\text{RT}}\right)$$

$$\eta_{\text{disl}} = \frac{1}{2}A^{\frac{1}{n}}(\dot{\varepsilon}_{\Pi})^{\frac{1-n}{n}}\exp\left(\frac{PV_a + E_a}{\text{nRT}}\right)$$

where $\dot{\varepsilon}_{\Pi}$ is the second invariant of the strain rate tensor; R gas constant, A pre-exponential factor, E_a activation energy, V_a activation volume, and n creep exponent.

The effective viscosity of the viscous deformation is determined by taking the harmonic average between diffusion and dislocation creep.

$$\eta_{\text{vis}} = \left(\frac{1}{\eta_{\text{diff}}} + \frac{1}{\eta_{\text{disl}}}\right)^{-1}$$

The plastic deformation abides by the Drucker-Prager yield criterion (e.g., Ranalli, 1995). The viscosity of this plastic deformation is calculated using the following formula:

$$\sigma_y = C_o + P\phi$$

$$\eta_{\text{plas}} = \frac{\sigma_y}{2\dot{\varepsilon}_{\Pi}}$$

where σ_y is yield stress, C_0 cohesion, ϕ effective internal friction coefficient.

The effective viscosity of rocks (η_{eff}) is determined by the minimum viscosity between viscous and plastic deformation.

$$\eta_{\text{eff}} = \min(\eta_{\text{vis}}, \eta_{\text{plas}})$$

3.3. Model Setup

We use large-scale models with physical dimensions of 2,000 × 400 km and numerical mesh of 721 × 231 nodal points. The grid resolution varies from 1 km × 0.5 km in the basin to 7 km × 5 km in the boundary region. Continental lithosphere is set from x = 0–400 km, x = 800–900 km and x = 1,600–2,000 km part of the model domain, which is composed of an upper felsic crust (15 km), a lower mafic crust (15 km), a lithospheric mantle layer (67.5 km), and a transitional part from x = 900–1,000 km and x = 1,500–1,600 km area. A 400-km wide basin is set from x = 400–800 km, which is composed of a sedimentary layer (1 km) atop of it. The inherited boudinage structure of the basin is simulated by sinusoidal limits between a felsic upper crust (10 km), a mafic lower crust (10 km) and an ultramafic lithospheric mantle layer (47.5 km). An oceanic lithosphere is set from x = 1,000–1,500 km, which consists of sedimentary layer (2.5 km), a basaltic crustal layer (5 km), and a lithospheric mantle layer (62.5 km). The lithospheric mantle is composed of dry olivine, below the lithospheric mantle is the asthenosphere mantle, which is prescribed with dry olivine rheology (Ranalli, 1995).

The boundary conditions include free slip on the top and left boundaries, while the bottom and right boundaries are permeable. An additional internal boundary velocity is prescribed on the overriding plate to force convergence in the subduction zone. A speed of 3 cm/yr is applied at a depth ranging from 22.5 to 120 km on the right boundary in models, aiming to push the right continental lithosphere leftward for more than 4 Myr to initiate subduction with >120 km convergence from the right upper plate. A 22.5-km low viscosity "sticky" ($\eta = 10^{18}$ Pa·s) air atop the crust is implemented to mimic free surface for the finite difference method (Crameri et al., 2012). For the temperature configuration of the continental lithosphere, a linear gradient is applied with constant temperature of 0°C and 1,300°C at the top and bottom boundaries of the lithosphere, respectively. The thermal gradient used within the asthenosphere is quasi-adiabatic (0.5°C/km, Katz et al., 2003). The visco-plastic thermo-mechanical parameters of each lithology are based on a list of laboratory experiments (Ranalli, 1995) (Table 1).

Table 1
Rock Parameters Used in the Numerical Experiment

Parameters	Continental upper crust/ Sediments	Continental lower crust	Oceanic crust	Mantle	Hydrated mantle/Weak zone
Flow Law Parameters[a]					
Rheology	Wet Quartzite	Felsic granulite	Plagioclase	Dry olivine	Wet olivine
Preexponential factor A ($Pa^n s$)	1.97×10^{17}	4.98×10^{20}	4.80×10^{22}	3.98×10^{16}	5.01×10^{20}
Exponent n	2.3	3.1	3.2	3.5	4.0
Activation energy E_a (J/mol)	1.54×10^5	2.43×10^5	2.38×10^5	5.32×10^5	4.70×10^5
Activation volume V_a (m^3/mol)	0	0	0	1.0	0.8
Critical stress σ_{crit} (Pa)	3×10^4	3×10^4	3×10^4	3×10^4	3×10^7
Plasticity					
Cohesion C (Pa)	$2e^7/2e^7$	$2e^7/2e^7$	$1e^6/1e^6$	$2e^7/2e^7$	$1e^6/1e^6$
Effective friction coefficient φ	0.6/0.3	0.6/0.3	0.01/0.01	0.6/0.6	0.0/0.0
Strain weakening onset/end	1.0/2.0	1.0/2.0	0.5/1.5	0.5/1.5	0.5/1.5
Material properties					
Density ρ (kg/m^3)[b,c]	2,750	2,850	3,000	3,300	3,300
Thermal expansion α (K^{-1})[d]	3×10^{-5}	3×10^{-5}	3×10^{-5}	3×10^{-5}	3×10^{-5}
Compressibility β (Pa^{-1})	1×10^{-11}	1×10^{-11}	1×10^{-11}	1×10^{-11}	1×10^{-11}
Heat capacity C_p (J/kg/K)[b]	1,000	1,000	1,000	1,000	1,000
Heat conductivity k[d]	$0.64 + 807/(T+77)$	$1.18 + 474/(T+77)$	$1.18 + 474/(T+77)$	$0.73 + 1{,}293/(T+77)$	$0.73 + 1{,}293/(T+77)$
Radioactive heating H_a (W/m^3)	2.0×10^{-6}	2.0×10^{-7}	2.2×10^{-7}	2.2×10^{-8}	2.5×10^{-8}
Solidus T_s (K)[e,f]	T_{s1}	T_{s2}	T_{s3}	T_{s4}	T_{s4}
Liquids T_l (K)[e,f]	T_{l1}	T_{l2}	T_{l3}	T_{l4}	T_{l4}

Note. $T_{s1} = 889 + 17{,}900/(P + 54) + 20{,}200/(P + 54)^2$ at $P < 1{,}200$ MPa or $831 + 0.06P$ at $P > 1{,}200$ MPa; $T_{l1} = 1262 + 0.09P$. $T_{s2} = 1327 + 0.0906P$; $T_{l2} = 1423 + 0.105P$. $T_{s3} = 973 - 70{,}400/(P + 354) + 778 \times 10^5/(P + 354)^2$ at $P < 1{,}600$ MPa or $935 + 0.0035P + 0.0000062P^2$ at $P > 1{,}600$ MPa; $T_{l3} = 1423 + 0.105P$. T_{s4} = KATZ2003; T_{l4} = KATZ2003. [a]Ranalli (1995) [b]Turcotte and Schubert (2002) [c]Bittner and Schmeling (1995) [d]Clauser and Huenges (1995) [e]Schmidt and Poli (1998) [f]Katz et al. (2003).

We set up 5 groups of models in total and tested 3 factors, including the wavelength of the basin (λ), thickness of the lithospheric of the basin (H) and the pushing velocity from the right converging upper plate (v). In Group 1, 12 models are set with λ = 38, 76, 152 km and ∞ (flat basin), v = 3, 5, 7 cm/yr, H = 67.5 km. In Group 2, 4 models are set with λ = 38, 152 km, v = 3, 7 cm/yr, H = 57.5 km, while Group 3 also contains 4 models sharing same design with Group 2 except the thickness of basin (H = 77.5 km). Group 4 uses the same parameters as Group 1, 2 and 3, but without pushing the right upper plate to initiate the subduction. Similarly, Group 5 is set without the pre-existing rifted basin and the push (no basin models). Besides, 36 markers are set in the basin to record the subsidence of it (Figure 2b).

3.4. Correction of the Isostasy and Boundary Condition

In our models, both isostasy and boundary condition contribute to the final basin subsidence. To isolate and quantify their respective influences, we use two specific model groups: Group 4, which includes only pre-existing basins but no subduction, and Group 5, which includes neither pre-existing basins nor subduction. To illustrate the contribution from these two factors, we select three representative models and compare their subsidence values. The first is a reference model (light blue line in Figure 3; shown in Figure 4a), which includes a pre-existing rifted basin (λ = 38 km) and ongoing subduction (v = 3 cm/yr). The second is a parallel model (brown line in Figure 3) from Group 4, which shares the same setup as the reference model but excludes subduction (v = 0 cm/yr), in order

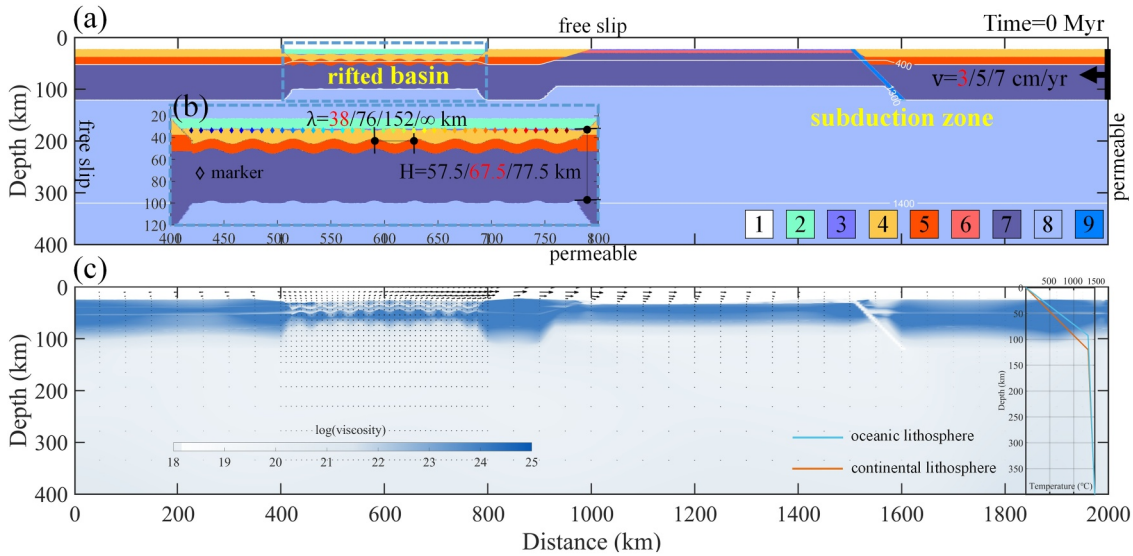

Figure 2. Initial setup of the reference model ($\lambda = 38$ km, $H = 67.5$ km, $v = 3$ cm/yr). (a) The initial design of the reference model shows the composition with zoomed window of the basin part in panel (b). (c) Viscosity field of the reference model at 0.016 Myr with geotherm for continental and oceanic lithosphere, respectively. In panel (a), white lines represent the 400°C, 1300°C, and 1400°C isotherms, while λ and H indicate the wavelength and thickness of the basin, respectively. 1 to 9 in material boxes in panel (a) refers to air, water, sediments, continental upper crust, continental lower crust, oceanic crust, lithospheric mantle, asthenospheric mantle and weak zone, respectively. Pentagrams with different colors in panel (b) refer to markers used to record the subsidence rate covering the whole basin.

to assess the effect of isostasy. The third is a static model (light red line in Figure 3) from Group 5, which lacks both the pre-existing basin and subduction, and is used to evaluate the effect of boundary conditions.

The subsidence values from each model—denoted S_2 (reference), S_1 (parallel), and S_0 (static)—are used to calculate tectonic subsidence (S_{tectonic}), as illustrated in Figure 3. Comparison of topography in Figure 3 from 0 to 0.52 Myr shows that all models experience uplift first. Yet, the static model has only ~1 km uplift of the topography, while reference and parallel model has >7 km uplift in average due to the existence of the basin under isostasy. However, the reference model still yields a lower surface elevation compared with the parallel model without subduction, highlighting that subduction can induce additional subsidence beyond that caused by isostasy and boundary conditions.

To extract only the contribution from subduction leading to tectonic subsidence in the basin, we set 36 markers at the same spatial positions covering the basement/continental surface to record the subsidence rate of all models. S_2, S_1 and S_0 refer to models with both pre-existing basin and subduction in Group 1 to 3, models with pre-existing basin but no subduction in Group 4, and models without pre-existing basin and no subduction in Group 5, respectively. With the evolution time (Δt) of models, the tectonic subsidence rate (S'_{tectonic}) from the subduction for each model is calculated according to:

$$S_{\text{tectonic}} = S_2 - S_1 - S_0,$$

$$S'_{\text{tectonic}} = S_{\text{tectonic}}/\Delta t.$$

To quantify the combined effects of the above three parameters H, v, and λ on the width of subsidence area (A), we defined a dimensionless number Cz, which is calculated according to:

$$Cz = v * \frac{H}{\lambda}.$$

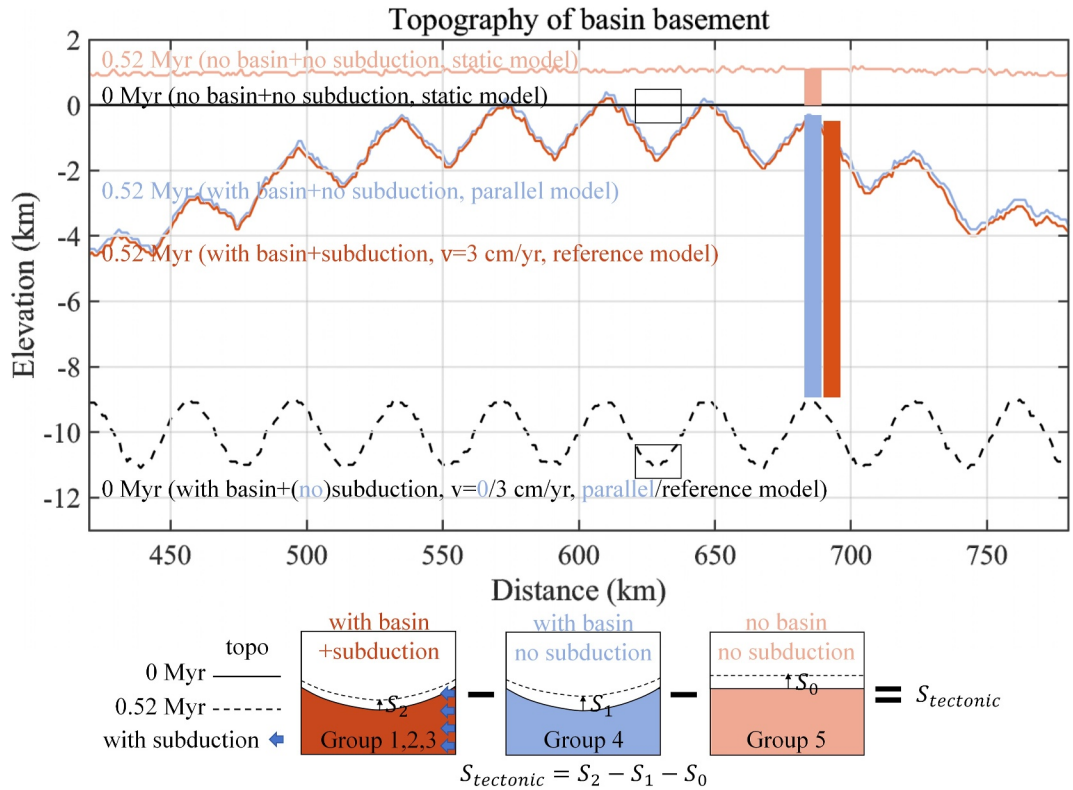

Figure 3. Topography of basin basement/continental surface in reference model, static model, and parallel model at 0 and 0.52 Myr. Solid and dotted black, brown, light red and light blue lines refer to the topography of the basin basement/continental surface in models with and without the pre-existing basin at 0 and 0.52 Myr, respectively, with zoomed area (black solid rectangle) showing the change of topography. S_2, S_1, S_0 refers to the subsidence value of basement/continental surface in reference model, parallel model and static model, respectively. S_{tectonic}, tectonic subsidence.

4. Experimental Results

4.1. Evolution of the Reference Model

The evolution of the reference model with $\lambda = 38$ km, $H = 67.5$ km, and $v = 3$ cm/yr is depicted in Figure 4. Specifically, Figure 4e delineates the subsidence of the rifted basin under compression from subduction in three phases, characterized by slow–fast–slow variations in tectonic subsidence rate. Phase 2 with rapid subsidence is also marked as "reactivation stage", it shares the same timespan as the initiation of the subduction (SI) from 0.7 to 2.1 Myr, and is characterized by an accumulation of sediments atop the basin basement. Notably, subsidence shown in Figure 4 includes the contribution from both isostasy and boundary conditions, which are later excluded in calculating the tectonic subsidence rate.

To visually highlight the impact of tectonic subsidence, we have selectively extracted data from 0.15 Myr onward for presentation. This selection is necessary because abnormal values caused by numerical disturbances arising from finite iterations during the initial stages prior to 0.15 Myr. We use a set of models (Group 1) with $\lambda = 38$ km, 76 km, 152 km and ∞ km (flat basin design), respectively, to assess the impact of λ ($H = 67.5$ km, and $v = 3$ cm/yr). The results from this group are illustrated in Figure 5, unequivocally demonstrating the following findings:

1. The tectonic subsidence rate of the markers can help identify 3 phases regardless of varying wavelength of the basin. An obvious rapid phase (Phase 2) featuring fast tectonic subsidence corresponds to "reactivation stage" from 0.7 to 2.1 Myr, while another two quieter phases (Phase 1 before 0.7 Myr and Phase 3 after 2.1 Myr) show rates close to 0 mm/yr rate before and after the reactivation stage. The reactivation stage (Phase 2) shares the same timespan as the reference model in Figure 4 under the same subduction velocity, indicating that the responses of the basin to the subduction depends mainly on the subuction velocity with constant timespan of this stage.

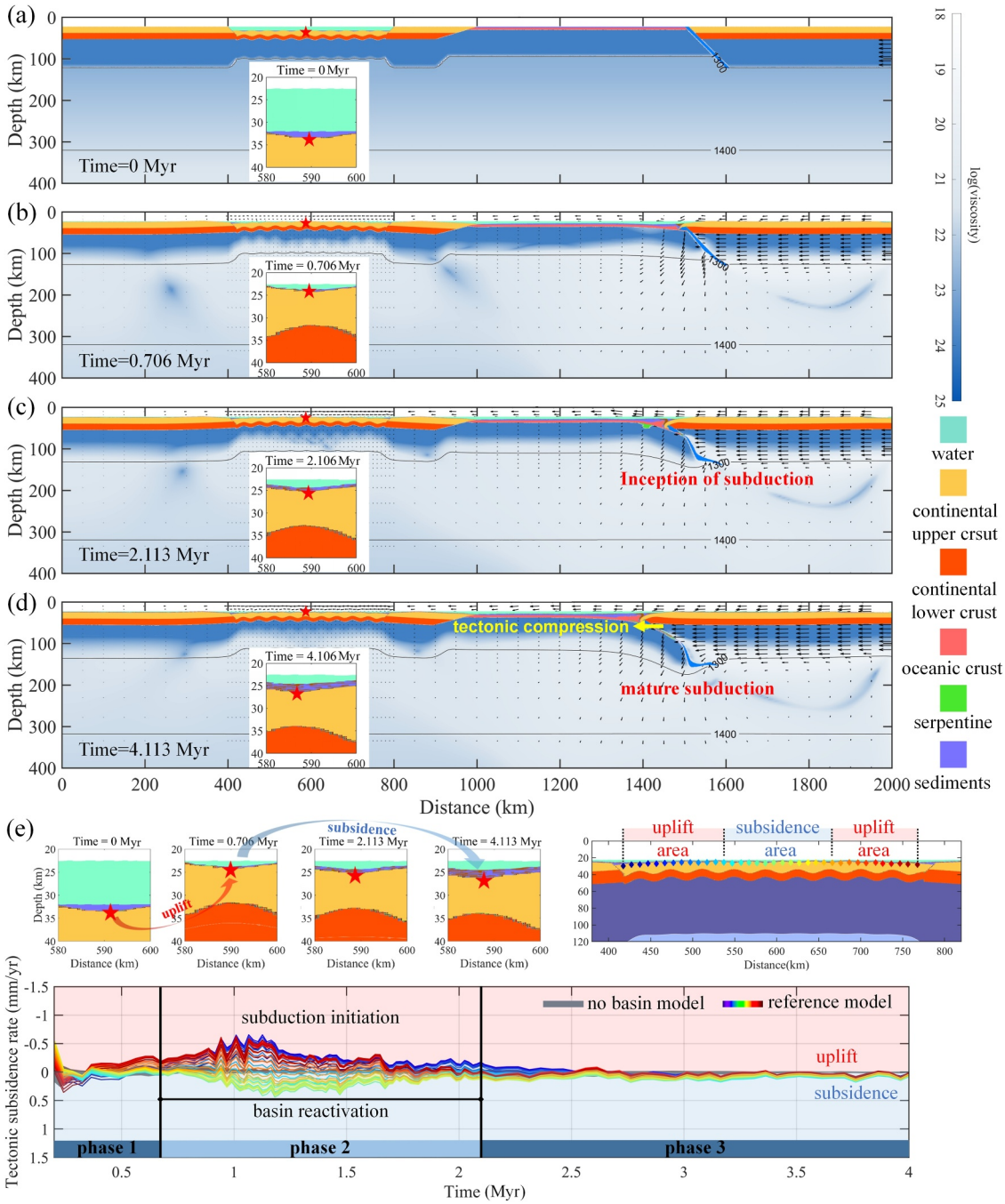

Figure 4. Evolution and tectonic subsidence rate of the reference model. (a–d) The compositional and viscosity field evolve at 0, 0.7, 2.1, and 4.1 Myr, see the position of the red pentagram in the left-up part of (e), black lines represent the 1300°C and 1400°C isotherms, black arrows respond to velocity direction and relative scale. (e) Movement of red pentagram in composition field and the tectonic subsidence rate of markers atop the basin basement with time, see the position of markers in the right-up zoomed composition field of the basin at 4.1 Myr, each line refers to the marker with the same color while the gray area behind them refers to the tectonic subsidence rate in model without the pushing velocity. Light red and blue areas in panel (e) refer to uplift and subsidy movement, respectively.

2. During the rapid phase featuring the reactivation stage, the line graphs in each model show that the tectonic subsidence rate of the markers in the central part of the basin is positive and can reach up to 0.5 mm/yr, while the rates on both flanks of the basin are negative. This indicates that the central part of the basin is subsiding while two flanks are uplifting, even under compression from subduction. Furthermore, the smaller the

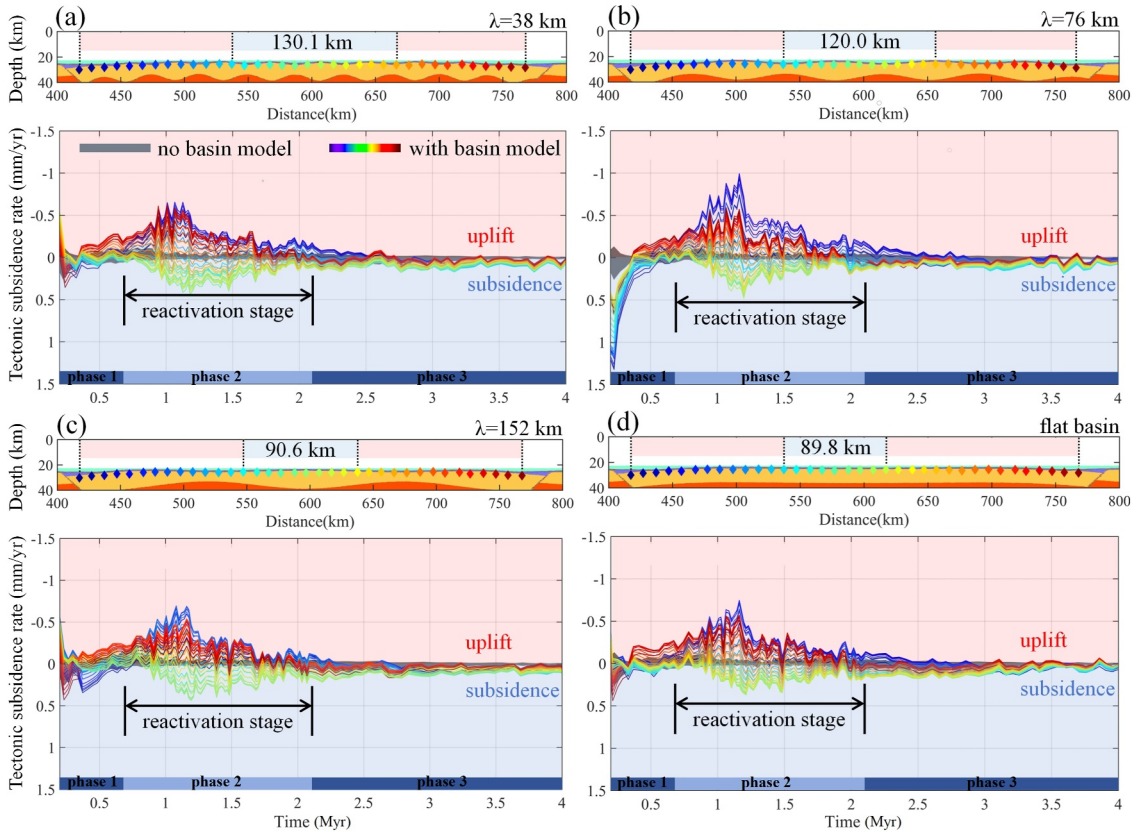

Figure 5. The comparison between the compositional design of the basin (color graphs) and the tectonic subsidence rate (line graphs) is presented in models with different wavelengths of the basin (λ = 38 km, 76 km, 152 km, and flat basin with $\lambda = \infty$ km) and no pre-existing basin model. Subgraphs (a–d) show the composition field of the basin at 4.1 Myr (color graphs) and the tectonic subsidence rate changes (line graphs) of markers with time. Each line of tectonic subsidence rate refers to markers with the same color in the composition field. Light blue and red areas in line graphs indicate the subsidy and uplift movements of markers, they are also employed to show the movements in different parts of the basin during the reactivation stage in the composition field (color graphs). Above models featuring H = 67.5 km and v = 3 cm/yr.

wavelength, the broader the subsiding area becomes (see the width of the light blue areas atop the composition subgraphs in Figure 5).

3. Before and after the reactivation stage, the tectonic subsidence rate of the markers in the basin is similar to that in the models without a pre-existing basin. The same timespan of the reactivation stage (from 0.7 to 2.1 Myr) is consistently reflected in all models with a basin. However, the reactivation stage only occurs when a pre-existing basin is present. In contrast, models without a basin show little variation in subsidence rate, which remains close to 0 throughout (see the gray area in each line graph in Figure 5). Here we propose that the reactivation stage of the tectonic subsidence rate is the response of the basin to subduction initiation, since they share the same timespan.

To sum up, the subsidence of the rifted basin under compression from the adjacent subduction during the SI stage can be recorded by the tectonic subsidence rate in different parts of the basin that feature a reactivation stage. The timespan of the reactivation stage is not related to the wavelength of the basin, but the wavelength of the basin determines the width of the subsiding area in the basin. Moreover, the reactivation stage ends until the inception of the subduction.

4.2. Parameter Effects on Tectonic Subsidence Rate

We test three factors with five groups of models, including the wavelength λ, the lithospheric thickness of basin H, and the pushing velocity of the right converging continental lithosphere v, to see their influence. The wavelength of the sub-basins (λ) is set to 38, 76, 152 km, and ∞ km (flat basin design) to represent different inherited boudinage structures of the basin, and the lithospheric thickness of basin (H) is set to 57.5, 67.5, and 77.5 km with

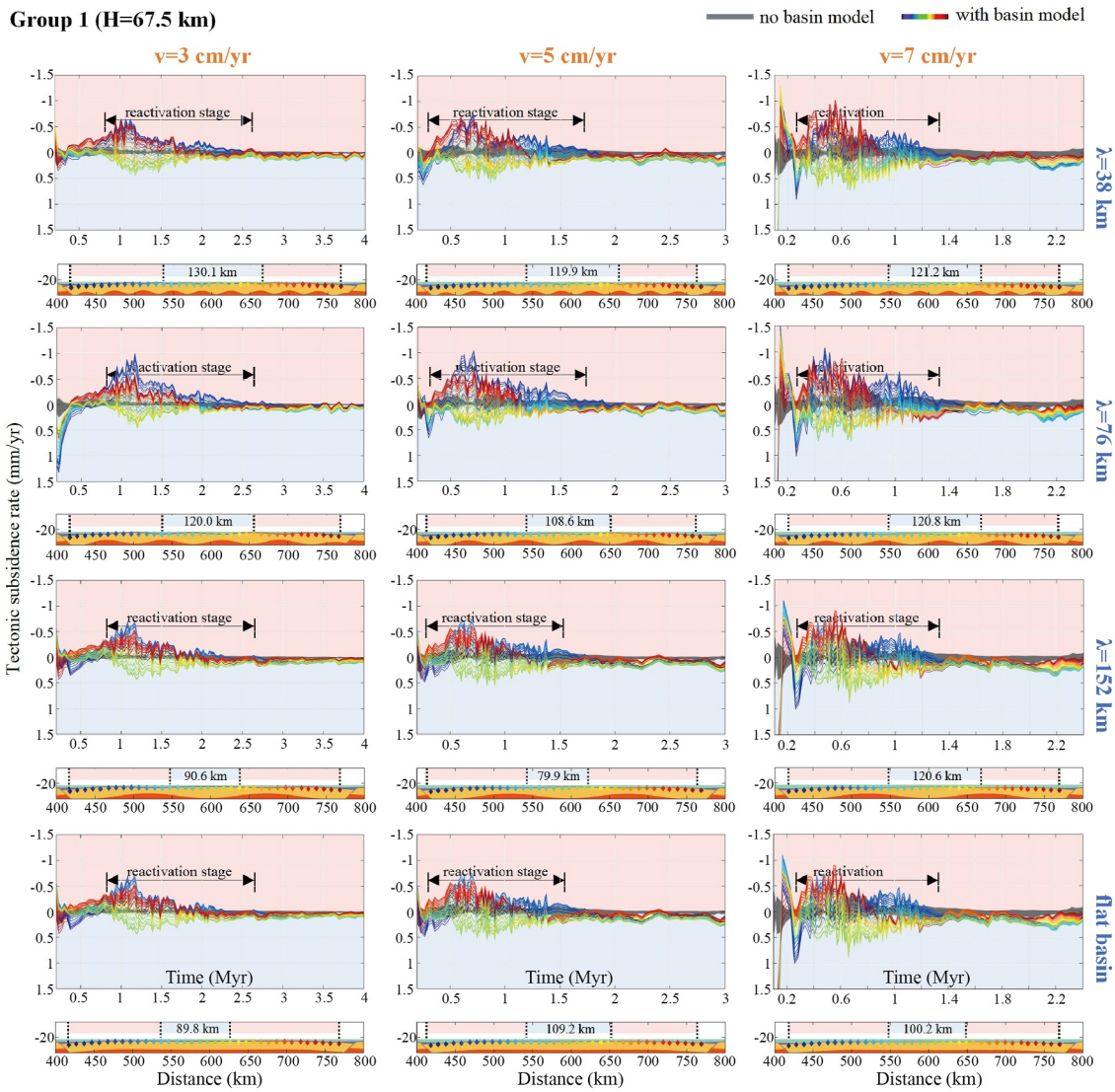

Figure 6. Results of Group 1 models. Lines with different colors refer to the markers with the same color in basin composition color graphs, indicating the tectonic subsidence rate of each marker. Gray areas in each subgraph refer to the tectonic subsidence rate observed in no pre-existing basin models. The width of the sinking area in each model during the reactivation stage is marked on the light blue area in each basin composition subgraph, while the light blue and red areas refer to the sinking and uplift areas, respectively.

corresponding changes in the upper crust, lower crust, and the lithospheric mantle that represents different strengths of the basin. The converging velocity (v) is set to 3, 5 and 7 cm/yr. Through the utilization of a subtractive approach to exclude the influence from isostasy and boundary conditions, we thoroughly examine the evolution process of the basin with subduction and quantify the tectonic subsidence rate in various regions of the basin with 36 markers covering the whole basin basement.

Group 1 (Figure 6) contains a series of models with different λ and ν values but with a constant thickness of basin (H = 67.5 km). Group 2 and 3 (Figures 7 and 8) both contain four end-member models with λ = 38/152 km and ν = 3/7 cm/yr, while models in Group 2 with the constant H = 57.5 km and Group 3 with the constant H = 77.5 km, respectively. To analyze the effects of the above parameters, we focus on the duration of the reactivation stage, the variation of markers' tectonic subsidence rate, and the width of the subsiding area in the basin during the reactivation stage.

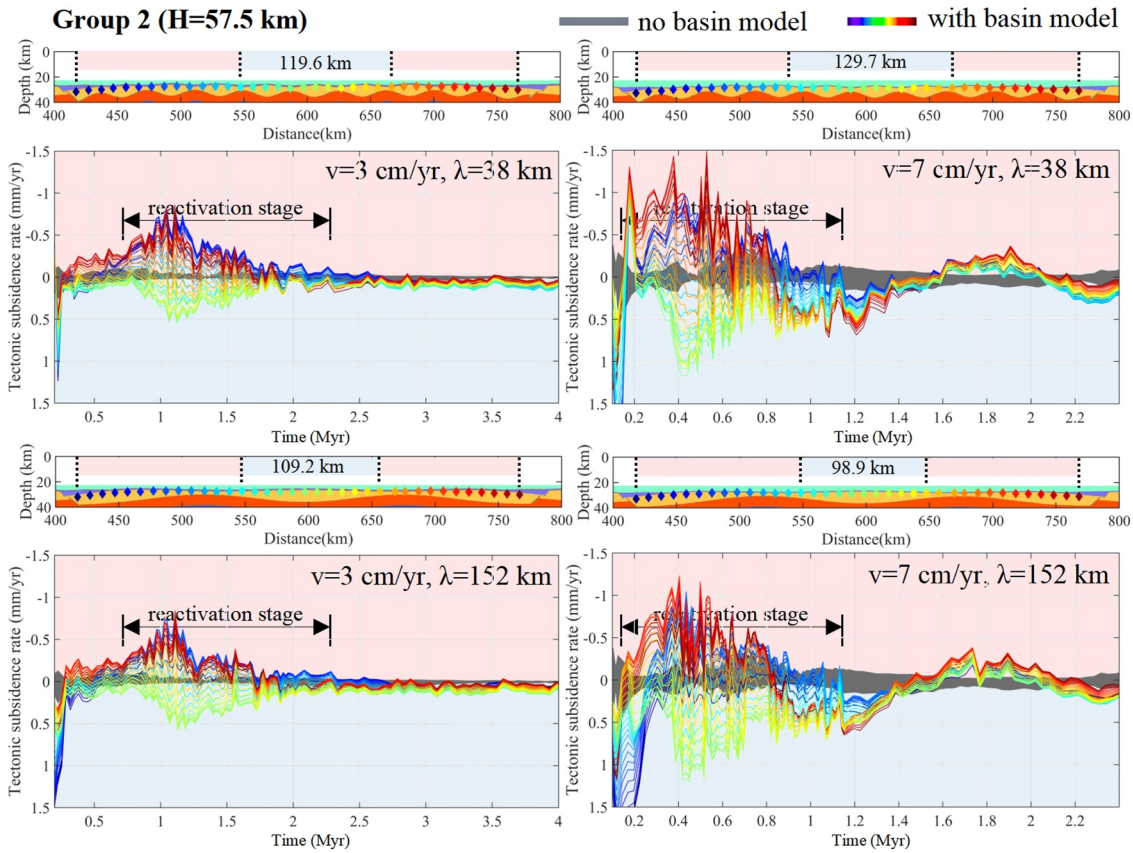

Figure 7. Results of models in Group 2. Lines with different colors refer to the markers with the same color in basin composition color graphs, indicating the tectonic subsidence rate of each marker. Gray areas in each subgraph refer to the tectonic subsidence rate observed in no pre-existing basin models. The width of the sinking area in each model during the reactivation stage is marked on the light blue area in each basin composition subgraph, while the light blue and red areas refer to the sinking and uplift areas, respectively.

4.2.1. The Effect of the Wavelength (λ) of the Basin and Velocity (V)

Twelve models in Group 1 are employed to test the effect of the wavelength of the basin and pushing velocity, with λ = 38/76/152 km and ∞ km (flat basin design), ν = 3/5/7 cm/yr cases representing the different inherited boudinage structures of the basin and subduction with different velocities (Figure 6). Here we conclude that:

1. With the same velocity of the converging upper plate, the subsidence area of the basin decreases with the increasing wavelength (λ), except in the flat basin model ($\lambda = \infty$). All models with the same wavelength share the same reactivation stage timespan. A smaller wavelength leads to more distributed deformation in the basin, resulting in a wider subsidence area, while a larger wavelength leads to a narrower subsidence area.
2. With the same wavelength of the basin, the duration of the reactivation stage decreases from around 1.4–1 Myr with increasing velocity. A more pronounced reactivation stage with a higher peak value of tectonic subsidence rate can be observed with increasing velocity (ν). Under relatively fixed horizontal boundary conditions, more deformation occurs in the vertical movement of the basin through rapid subsidence rate. A faster velocity also leads to a shorter duration of subsidence.
3. In models with ν = 7 cm/yr, we observe a distinctly larger variation in the tectonic subsidence rate of markers compared to the flat basin model. This may be due to the stronger change in force state caused by the fast subduction velocity after the reactivation stage.

4.2.2. The Effect of the Thickness (H) of the Basin

To examine the effect of the mechanical strength of the basin, we varied the lithospheric thickness of the basin. We set eight end-member models with H = 57.5/77.5 km, λ = 38/152 km, ν = 3/7 cm/yr in Group 2 and Group 3. Here we compare the results in Group 2 and Group 3 (Figures 7 and 8) to conclude that: (a) An increase in

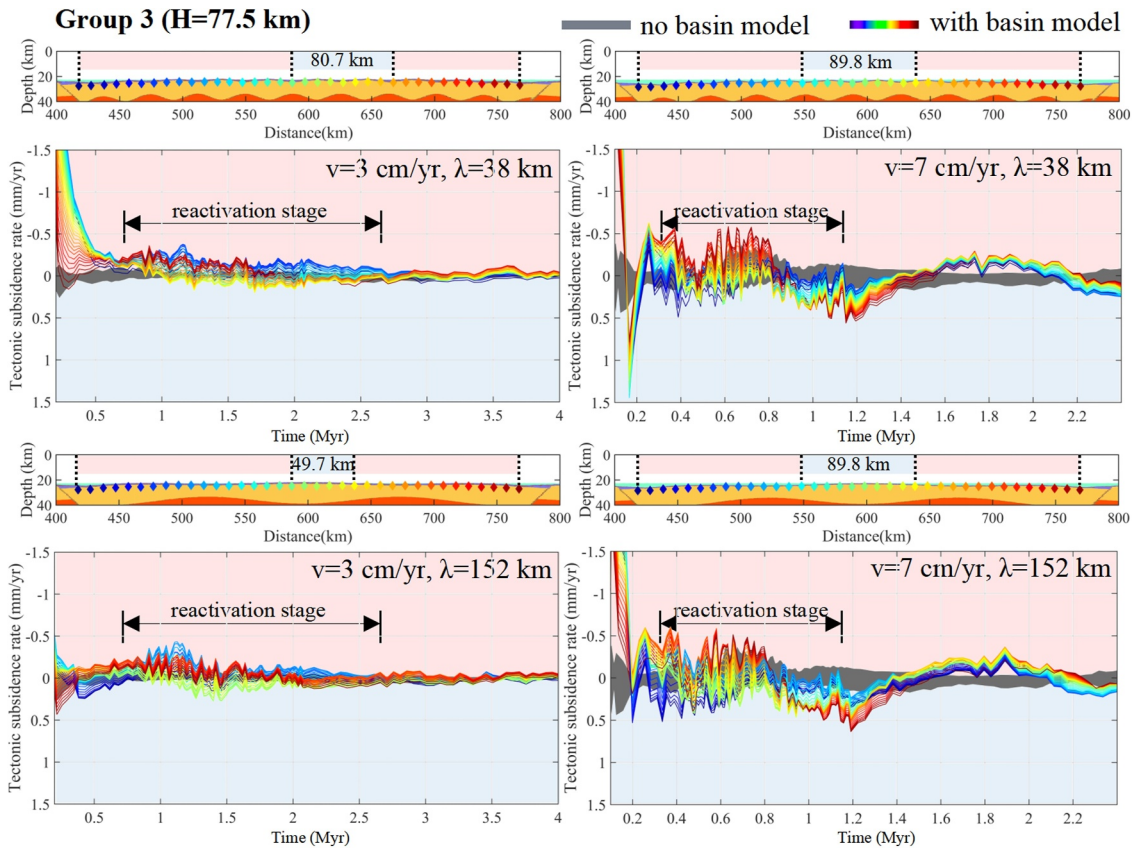

Figure 8. Results of models in Group 3 models. Lines with different colors refer to the markers with the same color in basin composition color graphs, indicating the tectonic subsidence rate of each marker. Gray areas in each subgraph refer to the tectonic subsidence rate observed in no pre-existing basin models. The width of the sinking area in each model during the reactivation stage is marked on the light blue area in each basin composition subgraph, while the light blue and red areas refer to the sinking and uplift areas, respectively.

thickness efficiently shortens the width of the subsiding area in the basin, the maximum and minimum values decrease from 129.7 to 89.9 km and from 98.8 to 49.7 km, respectively; (b) The tectonic subsidence rate during the reactivation stage is almost reduced by half on average with 20 km increase in thickness (H). (c) A longer reactivation stage is observed in Group 3 results, which lasts about 2 Myr with $\nu = 3$ cm/yr, while this duration is approximately 1.6 Myr in Group 2.

Above all, a basin with a greater H or λ exhibits a narrower subsiding area, a smaller variation in tectonic subsidence rate, and a longer reactivation stage. Besides, we also see a larger variation among markers in the tectonic subsidence rate after the reactivation stage in models with $\nu = 7$ cm/yr. Analysis of wavelength (λ), velocity (ν), and thickness (H) shows that:

1. The duration of the reactivation stage remains constant across models, while higher velocity increases subsidence intensity and shortens this stage due to enhanced vertical deformation under fixed horizontal boundaries.
2. The reactivation stage is largely independent of basin geometry, suggesting that its persistence reflects subduction-driven forcing rather than structural inheritance.
3. The width of the subsiding area decreases with increasing λ and H, as thicker or longer wavelength basins are mechanically stronger and more resistant to deformation.

In summary, velocity controls the rate and duration of subsidence, whereas wavelength and thickness govern its distribution and magnitude by modulating basin strength.

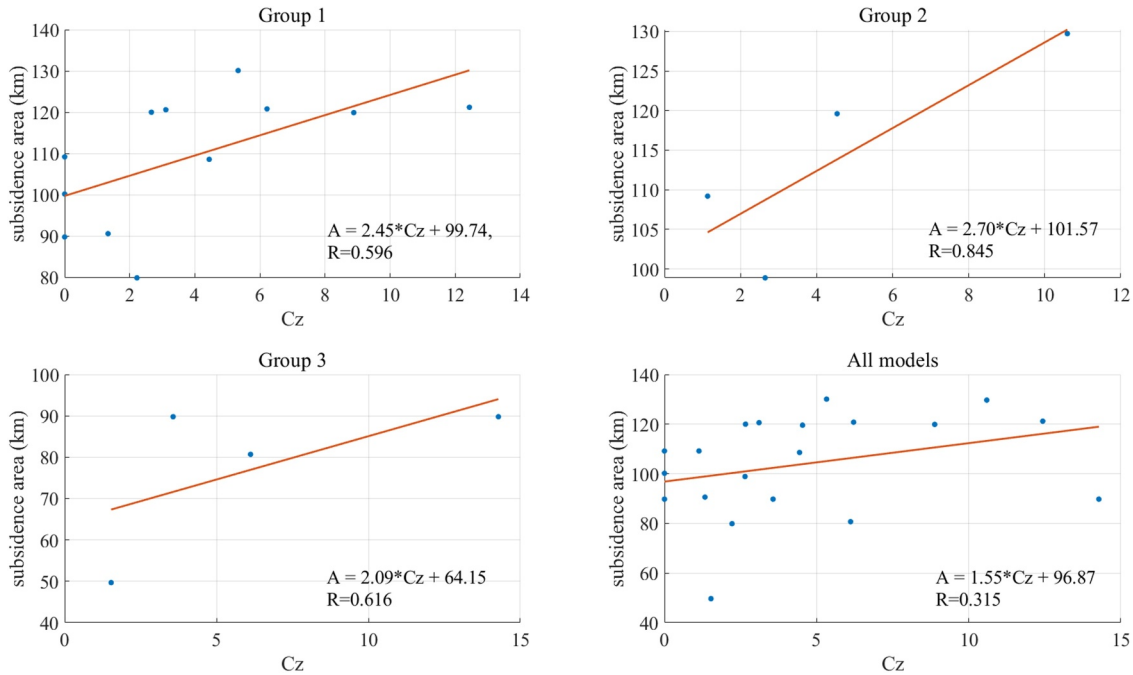

Figure 9. Correlation between tested factors and the width of subsidence area in the basin with fitting formula of models in different group. *A*, width of subsidence area in the basin; *Cz*, dimensionless number considering *H*, *v*, and *λ* (thickness of the basin, pushing velocity from the upper converging plate and wavelength of the basin). *R*, Pearson correlation coefficient.

4.2.3. Quantitative Analysis Between Width of Subsidence Area and 3 Tested Factors

To quantify the combined effects of the three tested parameters (*v*, *λ*, and *H*), we calculated the dimensionless number *Cz* for all models in groups 1–3 and compared it with the width of the subsiding area (*A*) (Figure 9).

From results in Figure 9 shows that *A* and *Cz*, are linearly correlated with *R* (Pearson correlation coefficient) ranging from 0.596 to 0.845 in separate group and 0.315 in all models group. The linear relationship between *Cz* and *A* indicates that the width of the subsidence area strongly depends on the tested factors (*H*, *v*, and *λ*). A positive correlation between *A* and *Cz* is evident with $R > 0.5$ in Groups 1,2,3, and this relationship can be still found in all models group even with smaller $R = 0.315$.

According to the definition of *Cz*, *λ* is negatively correlated with the final width of the subsidence area (*A*), whereas *H* and *v* are positively correlated with *A*. *H*, *λ* refer to the inherited structure of the basin from continental rifting, indicating that inherited boudinage structure with varying thickness and wavelength contribute to the basin inversion results calibrated by *A*. Pushing velocity (*v*) as a tectonic factor also contributes to the final width of the subsidence area during basin inversion, showing a positive correlation. *Cz* therefore provides an efficient way to link inherited boudinage geometry and tectonic forcing in describing basin inversion under subduction-related compression.

5. Discussion

5.1. Comparison of Subsidence Rate Between Models and Observations in PRMB

To compare our models' results with observations, we have gathered tectonic subsidence rate data of the PRMB from 30 Ma to the present (He et al., 2017; Liao et al., 2011; Ma et al., 2020; Tang et al., 2017; Xie et al., 2021), as illustrated in Figure 1c. Figure 1c clearly shows that there is a significant increase in tectonic subsidence rate from 25 Ma to 13 Ma. During this period, the tectonic subsidence rate exceeded 0.3 mm/yr and persisted for over 1 Myr in different data sets. However, the cause of this puzzling subsidence in the PRMB remains unclear.

In our models, the results indicate that the tectonic subsidence rate can be positive and persist for >1 Myr, reaching over 0.4 mm/yr, indicating that the basin subsides in the context of forced subduction initiation. These

results are consistent with the anomalous subsidence observed during basin inversion in the PRMB, which shows a positive tectonic subsidence rate across nearly the entire basin area (see Figure 1c), corresponding to the central part of the basin in our models. We conclude that the central part of the basin experienced a secondary phase of post-rift subsidence driven by tectonic compression induced by the Manila Subduction. Unlike the findings of Li et al. (2021), which require a thin initial crustal thickness (<7 km) after extension to explain the rapid post-rift subsidence in the northern part of the SCS, our models do not require excessive thinning of the continental lithosphere.

Consequently, we propose that the Manila Subduction is likely responsible for the anomalous subsidence observed in the PRMB and associated basin inversion structures (Sun et al., 2014; Wang et al., 2025). The consistency of timespan between the reactivation stage and inception of the subduction may help identify the SI of the Manila Subduction, as discussed in Section 5.3.

5.2. Difference of Modes Between Our Models and Observations in Other Examples

Anomalous subsidence is also widely observed around the world, including southern Sundaland, the Kurile Basin, southern California and the Pannonian Basin (Baranov et al., 2002; Oravecz et al., 2024; Yang et al., 2016; Yeats, 1978), but scenarios in these areas are attributed to the horizontal displacement under compression, the regional stress distribution, downwelling mantle flow, and slow pushing velocity, respectively. Both the Kurile Basin (Baranov et al., 2002) and southern California (Yeats, 1978) with rapid subsidence is attributed to the Pacific Subduction induced regional compressional stress, but the Kurile Basin with volcanism joining in the process and making it more complicated. Besides, the southern California Basin is a strike-slip basin (Yeats, 1978), while the Kurile Basin, Pannonian Basin (Oravecz et al., 2024) and Sundaland (Yang et al., 2016) are rifted basins formed in back-arc extension state and adjacent to subduction. In these examples, we can see that tectonic events can't be neglected, and especially in southern Sundaland, subduction is also employed to explain the occurrence of downwelling mantle flow that brings the subsidence (Yang et al., 2016). Comparing these examples, we see that the compression from the subduction with inherited boudinage structure is overlooked in former researches. Another model studying the PRMB still focuses on the basin part solely with changing boundary condition (Li et al., 2021), but including varying stretching degree and tectonic quiescence leading to different inherited structure of the basin since continental rifting.

While former models only considered subduction and neglected the detailed inherited structure of the basin (Yang et al., 2016), or successfully reproduced different structures of the basin (Li et al., 2021) but still overlooked the influence from subduction leading to tectonic subsidence, or merely proposed that the pushing velocity in the first order controls the occurrence of subsidence or not, without considering the source of tectonic compression (Oravecz et al., 2024), the design of our models integrates these setups. We conclude that the inherited structure of the basin and varying pushing velocity from subduction are crucial factors. Based on this novel design, our study provides detailed results compared to former models. For instance, the rifted basin exhibits both uplift and subsidence areas depending on the inherited boudinage structure with varying wavelength and thickness. The central part of the basin always subsidies with high tectonic subsidence rate (>0.4 mm/yr), while the two flanks uplift. Additionally, we surprisingly found that subduction initiation (SI) coincides with the reactivation stage of the basin's central part under tectonic compression from the subduction. This further indicates that anomalous subsidence in the rifted basin can be linked to the SI, see more discussion in Section 5.3.

5.3. Implications for the Identification of SI in the Manila Subduction Zone

In our reference model, we have observed a consistent reactivation stage spanning from 0.7 to 2.1 Myr with peak value of tectonic subsidence rate in basin's central part, believed to be the response of the rifted basin to the SI of the Manila Subduction. However, such a stage is absent in model without the pre-existing rifted basin (Figure 4). Upon comparing the tectonic subsidence rates between our models and observations, we noticed that within the PRMB there exists a peak of tectonic subsidence rate from preferred data set with highest time-resolution (Tang et al., 2017), lasting for 1∼2 Myr from ∼18 to ∼16 Ma (Figure 10a). This peak timespan is coincident with 1∼2 Myr timespan of the reactivation stage in our reference model, and it is attributed to the inception of the subduction from the comparison with no basin model (Figure 10c).

The PRMB began continental rifting during the Cenozoic, with the SCS starting to spread in the southern part of the PRMB at ∼32 Ma and ceased at ∼15 Ma (Barckhausen et al., 2014). During the SCS spreading, it collided

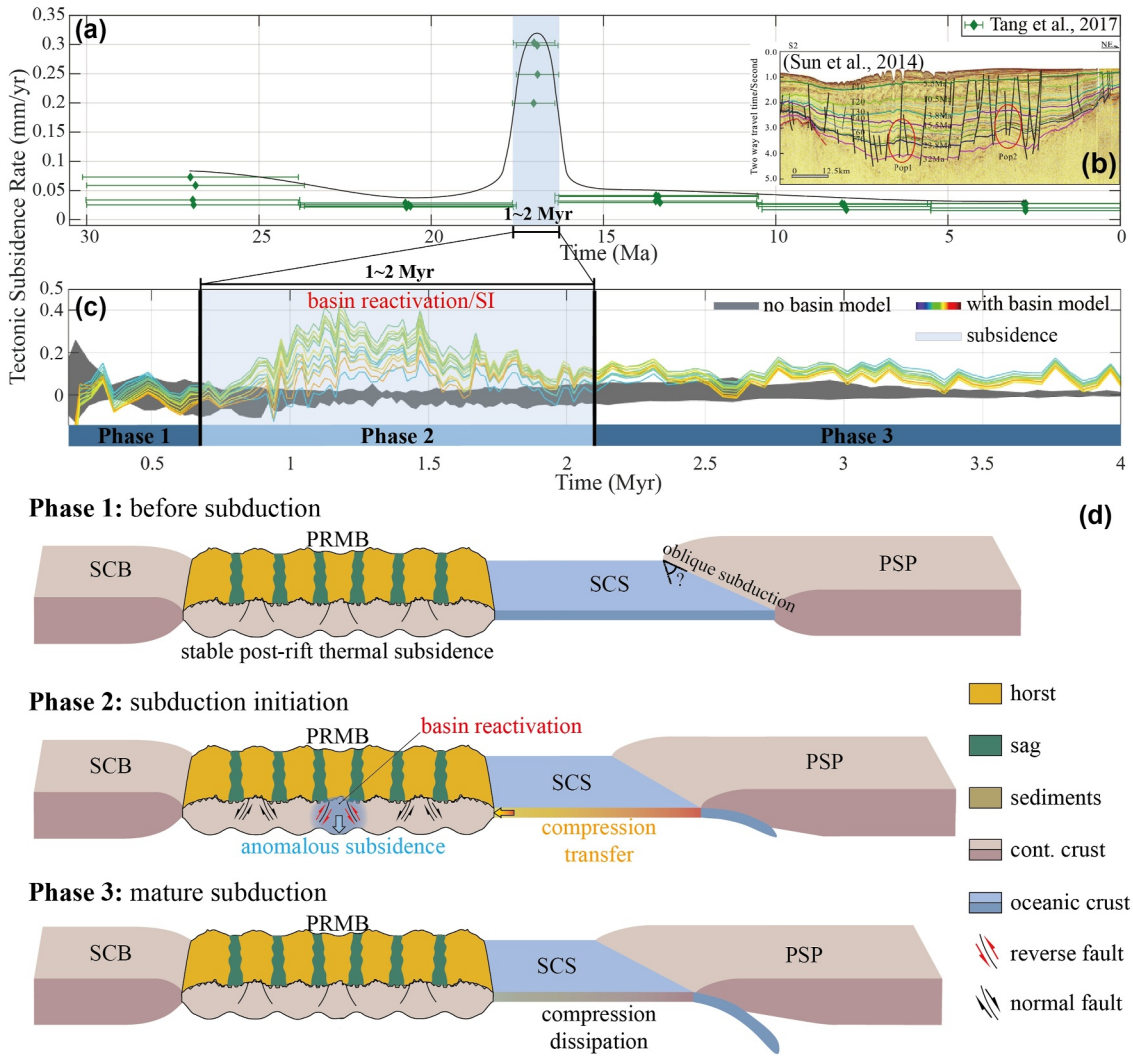

Figure 10. Comparison between reference model's results and data from the PRMB, and cartoon showing the subsidence of the rifted basin caused by the subduction process. (a) Preferred data set (Tang et al., 2017) with highest time-resolution and a peak lasting 1∼2 Myr from ∼18 to ∼16 Ma. (b) Pop-ups (pop1, pop2 in red circles) after 32 Ma, together with overlying sediments ranging from 23.8 Ma to 15.5 Ma and obviously thinner than wing areas, indicate basin inversion (Sun et al., 2014). (c) Reference model's tectonic subsidence rate with a peak lasting 1∼2 Myr in basin's central part. (d) Concept figure showing that after subduction initiation (SI), the central part of the rifted basin sinks under the compression transferred from the converging upper plate (PSP). PRMB-Pearl River Mouth Basin, PSP-Philippine Sea Plate, SCB-South China block, SCS-South China Sea.

with the PSP and subsequently subducted under it at different time along the subduction front (Wu et al., 2016). The tectonic compression force direction between the MSZ and PRMB changes over time in 3D, this may explain the varying timespans of the tectonic subsidence peak from different data sets observed in the PRMB (Figure 1b). Consequently, this variation in tectonic compression force direction contributes to different parts of the PRMB exhibiting distinct starting times for their responses. We discuss the influence of oblique compression during basin inversion in Section 5.4 in detail. Furthermore, here we propose that the anomalous tectonic subsidence of the basin reflects the SI of Manila Subduction. The consistence of a peak in tectonic subsidence rate between reference model and observations (Tang et al., 2017) indicates that the SI of the Manila Subduction may start from ∼18 to ∼16 Ma with 3 phases (Figures 10a and 10c). While the peak of tectonic subsidence rate appears in Phase 2 with basin reactivation, but slow subsidence in Phase 1 and Phase 3. Liu et al. (2020) concluded that the SI time of Manila Subduction varies from early Miocene to late Oligocene based on former researches, which is consistent with ∼18 Ma to ∼16 Ma proposed from tectonic subsidence rate, and also proposed that the SI time of the SCS started >9 Ma with ridge subduction, but with nonclear origin of diorite examples aging ∼26.8 to 15.5 Ma (overlaps with the subduction of the SCS) from Central Cordillera. Based on the consistence between our

reference model's results and observations, this finding further highlights that by considering the starting time of anomalous tectonic subsidence, we can identify the SI precisely and gain valuable insights for plate reconstruction. Former researches mainly used SSZ ophiolite and metamorphic soles to identify SI (Soret et al., 2017), while the subduction initiation is a short-lasting process compared to the whole subduction process, and it is difficult to observe rock records (Zhong & Li, 2019). Here we propose that the anomalous subsidence of the basin is the response to the Manila Subduction, and we can use the timespan of the reactivation stage, which features high tectonic subsidence rate lasting for >1 Myr, in the basin to identify the SI depending on the precision of results (Figures 10a and 10c).

5.4. Limitations and Perspectives

In our 2D models, we simplify the sedimentation and erosion processes using the functions described in Section 3.1 (Gerya & Yuen, 2003), and we calibrate the basin with varying wavelength and thickness to represent changes in total strength. This simplification and calibration are reasonable in this study, which focuses on tectonic subsidence in basins with varying inherited boudinage structures from continental rifting. There are other numerical models designed to study the subsidence in the rifted basin. In the case of the Pannonian Basin, Oravecz et al. (2024) focused on basin subsidence during inversion by considering the influence of thermal subsidence and sedimentation, thereby employing a more complex surface process. Another model for the PRMB is from Li et al. (2021), which mainly studied the hyper-thinned continental crust in the PRMB (<10 km) and therefore designed a narrower basin structure, although most parts of the PRMB feature a 15∼25 km thick continental crust (Cameselle et al., 2020; Deng et al., 2020; Zhang et al., 2023) and the total width of the PRMB varies from ∼300 to ∼ 600 km according to different directions. Our model setup considers a broader tectonic setting and therefore employs a wider basin structure (∼400 km in width). We focus primarily on tectonic subsidence caused by tectonic events, and thus exclude the influence of surface processes such as sedimentation and erosion. We also propose that incorporating a more complex and realistic surface process, and a more realistic continental margin design with varying thickness of the basin's thinned area, along with variable basin width, could provide a more comprehensive understanding of the final results—an aspect that can be explored in future work.

In addition, an oblique compression due to the change of subduction front direction may also influence the deformation of the rifted basin. Granado et al. (2017) built 3D analog models to study basin inversion with inherited faults and oblique compression with burial (sediments), showing that basin accommodates strain and then new faults form, rather than with deformation following inherited faults but rift structure with distributed deformation. It is consistent with 2D numerical models results from Lafosse et al. (2016) indicating that basins are more reactivated than faults with burial. Brun and Nalpas (1996) also shows that in 3D, when oblique compression is set to the basin with high angle (>45°), basement normal faults are predominately reactivated as strike-slip faults, whereas newly formed thrust faults accommodate the shortening perpendicular to the grabens. In our 2D models, due to the limitation of reconstructions' resolution, exact proto-direction of subduction front and the position of the PRMB during subduction are hard to constrain. Based on former researches mentioned above, we see that it is the basin's structure that matters to the final deformation pattern of the basin, including subsidence and uplift, even under oblique compression, 2D models can still work with low oblique compression (<45°) neglecting the influence of strike-slip in 3D. Our model considering a rifted basin and subduction may also work for other cases, like the Pannonian Basin, which also features rifting history and then under compression due to subduction.

Finally, due to the complexity of the Manila Subduction, this study only focus on the interactions between the SI of it and the anomalous subsidence observed in the PRMB. With the ongoing of Manila Subduction, there are scenarios including double volcanic chains (Kawamoto et al., 2013; Cheng et al., 2019; Pan & He, 2023), slab window and slab detachments (Fan et al., 2015) after the inception of it. The interactions between long term subduction and the responses of the PRMB to it is still enigmatic, we believe this is an interesting topic and can be explored in the future.

6. Conclusions

We conducted a series of models with varying wavelength and lithospheric thickness of the rifted basin, and the pushing velocity of the converging upper plate to study the anomalous subsidence in the PRMB under compression from the Manila Subduction. Our results show that:

1. A "reactivation stage" with violent fluctuations of tectonic subsidence rate, which lasts for >1 Myr, can be identified. During this stage, central part of the basin can subsidy with high rate (>0.4 mm/yr) while two flanks uplift, and this stage is temporally consistent with the initiation of the subduction.
2. In the first order, it is the inherited boudinage structure of the basin coupled with the tectonic compression from the subduction that brings the anomalous subsidence in the central part of the basin, and this rule still works well even with varying subduction velocity and the change of basin's structure (thickness and wavelength of the basin) with positive correlation between these factors and basin's subsidence area width.
3. Our results have a good consistency with the observed enigmatic anomalous subsidence in the PRMB, and here we propose that it may help identify the initiation time of the Manila Subduction, and with the help of tectonic subsidence rate, we may identify the SI more precisely.

Conflict of Interest

The authors declare no conflicts of interest relevant to this study.

Data Availability Statement

All related data of the numerical models are provided in Zenodo (Zhou et al., 2023). Free software packages Generic Mapping Tools version 6 (Wessel et al., 2013) and Matplotlib (Hunter, 2007), are used for creating the figures.

Acknowledgments
Jie Liao acknowledges funding from the NSFC project (42222406). Here we would like to express our gratitude to Taras Gerya for providing the codes, and appreciate the discussion and advice from Shaoping Lu, Chen Cai and Sebastian Wolf. We also thank the two reviewers for their valuable comments and advice!

References

Arculus, R. J., Ishizuka, O., Bogus, K. A., Gurnis, M., Hickey-Vargas, R., Aljahdali, M. H., et al. (2015). A record of spontaneous subduction initiation in the Izu–Bonin–Mariana arc. *Nature Geoscience*, *8*(9), 728–733. https://doi.org/10.1038/ngeo2515

Baranov, B. V., Werner, R., Hoernle, K. A., Tsoy, I. B., vanden Bogaard, P., & Tararin, I. A. (2002). Evidence for compressionally induced high subsidence rates in the Kurile Basin (Okhotsk Sea). *Tectonophysics*, *350*(1), 63–97. https://doi.org/10.1016/S0040-1951(02)00081-1

Barckhausen, U., Engels, M., Franke, D., Ladage, S., & Pubellier, M. (2014). Evolution of the South China Sea: Revised ages for breakup and seafloor spreading. *Marine and Petroleum Geology*, *58*, 599–611. https://doi.org/10.1016/j.marpetgeo.2014.02.022

Bittner, D., & Schmeling, H. (1995). Numerical modelling of melting processes and induced diapirism in the lower crust. *Geophysical Journal International*, *123*(1), 59–70. https://doi.org/10.1111/j.1365-246X.1995.tb06661.x

Bonini, M., Sani, F., & Antonielli, B. (2012). Basin inversion and contractional reactivation of inherited normal faults: A review based on previous and new experimental models. *Tectonophysics*, *522–523*, 55–88. https://doi.org/10.1016/j.tecto.2011.11.014

Briais, A., Patriat, P., & Tapponnier, P. (1993). Updated interpretation of magnetic anomalies and seafloor spreading stages in the South China Sea: Implications for the tertiary tectonics of Southeast Asia. *Journal of Geophysical Research*, *98*(B4), 6299–6328. https://doi.org/10.1029/92JB02280

Brun, J. P., & Nalpas, T. (1996). Graben inversion in nature and experiments. *Tectonics*, *15*(3), 677–687. https://doi.org/10.1029/95TC03853

Buchanan, P. G., & McClay, K. R. (1991). Sandbox experiments of inverted listric and planar fault systems. *Tectonophysics*, *188*(1–2), 97–115. https://doi.org/10.1016/0040-1951(91)90317-L

Buiter, S. J. H., Pfiffner, O. A., & Beaumont, C. (2009). Inversion of extensional sedimentary basins: A numerical evaluation of the localisation of shortening. *Earth and Planetary Science Letters*, *288*(3–4), 492–504. https://doi.org/10.1016/j.epsl.2009.10.011

Cameselle, A. L., Ranero, C. R., & Barckhausen, U. (2020). Understanding the 3D formation of a wide rift: The central South China Sea rift system. *Tectonics*, *39*(12), e2019TC006040. https://doi.org/10.1029/2019TC006040

Cheng, Z., Ding, W., Faccenda, M., Li, J., Lin, X., Ma, L., et al. (2019). Geodynamic effects of subducted seamount at the manila trench: Insights from numerical modeling. *Tectonophysics*, *764*, 46–61. https://doi.org/10.1016/j.tecto.2019.05.011

Clauser, C., & Huenges, E. (1995). Thermal conductivity of rocks and minerals. *Rock physics and phase relations: a handbook of physical constants*, *3*, 105–126.

Cloetingh, S., & Burov, E. (2011). Lithospheric folding and sedimentary basin evolution: A review and analysis of formation mechanisms: Lithospheric folding and sedimentary basin evolution. *Basin Research*, *23*(3), 257–290. https://doi.org/10.1111/j.1365-2117.2010.00490.x

Cooper, M. A., Williams, G. D., de Graciansky, P. C., Murphy, R. W., Needham, T., de Paor, D., et al. (1989). Inversion tectonics — A discussion. *Geological Society, London, Special Publications*, *44*(1), 335–347. https://doi.org/10.1144/GSL.SP.1989.044.01.18

Crameri, F., Tackley, P. J., Meilick, I., Gerya, T. V., & Kaus, B. J. P. (2012). A free plate surface and weak oceanic crust produce single-sided subduction on Earth: SINGLE-SIDED subduction on earth. *Geophysical Research Letters*, *39*(3). https://doi.org/10.1029/2011GL050046

Dai, L., Li, S., Lou, D., Liu, X., Suo, Y., & Yu, S. (2014). Numerical modeling of late Miocene tectonic inversion in the Xihu Sag, East China Sea Shelf Basin, China. *Journal of Asian Earth Sciences*, *86*, 25–37. https://doi.org/10.1016/j.jseaes.2013.09.033

Del Ventisette, C., Montanari, D., Sani, F., & Bonini, M. (2006). Basin inversion and fault reactivation in laboratory experiments. *Journal of Structural Geology*, *28*(11), 2067–2083. https://doi.org/10.1016/j.jsg.2006.07.0121

Deng, H., Ren, J., Pang, X., Rey, P. F., McClay, K. R., Watkinson, I. M., et al. (2020). South China Sea documents the transition from wide continental rift to continental break up. *Nature Communications*, *11*(1), 4583. https://doi.org/10.1038/s41467-020-18448-y

Fan, J. K., Wu, S. G., & Spence, G. (2015). Tomographic evidence for a slab tear induced by fossil ridge subduction at manila trench, South China Sea. *International Geology Review*, *57*(5–8), 998–1013. https://doi.org/10.1080/00206814.2014.929054

Franke, D., Savva, D., Pubellier, M., Steuer, S., Mouly, B., Auxietre, J. L., et al. (2014). The final rifting evolution in the South China Sea. *Marine and Petroleum Geology*, *58*, 704–720. https://doi.org/10.1016/j.marpetgeo.2013.11.020

Frimmel, H. E., & Fölling, P. G. (2004). Late vendian closure of the adamastor ocean: Timing of tectonic inversion and syn-orogenic sedimentation in the Gariep Basin. *Gondwana Research*, *7*(3), 685–699. https://doi.org/10.1016/S1342-937X(05)71056-X

Fyhn, M. B. W., Pedersen, S. A. S., Boldreel, L. O., Nielsen, L. H., Green, P. F., Dien, P. T., et al. (2010). Palaeocene–early Eocene inversion of the Phuquoc–Kampot Som Basin: SE Asian deformation associated with the suturing of Luconia. *Journal of the Geological Society*, *167*(2), 281–295. https://doi.org/10.1144/0016-76492009-039

Gerya, T. (2011). Future directions in subduction modeling. *Journal of Geodynamics*, *52*(5), 344–378. https://doi.org/10.1016/j.jog.2011.06.005

Gerya, T. V., & Yuen, D. A. (2003). Rayleigh–Taylor instabilities from hydration and melting propel 'cold plumes' at subduction zones. *Earth and Planetary Science Letters*, *212*(1–2), 47–62. https://doi.org/10.1016/S0012-821X(03)00265-6

Glennie, K. W., Boegner, P. L. E., Illing, L. V., & Hobson, G. D. (1981). *Petroleum geology of the continental shelf of north-west Europe* (pp. 110–120). Institute of Petroleum.

Granado, P., Ferrer, O., Muñoz, J. A., Thöny, W., & Strauss, P. (2017). Basin inversion in tectonic wedges: Insights from analogue modelling and the Alpine-Carpathian fold-and-thrust belt. *Tectonophysics*, *703–704*, 50–68. https://doi.org/10.1016/j.tecto.2017.02.022

Gurnis, M., Hall, C., & Lavier, L. (2004). Evolving force balance during incipient subduction: Evolving force balance. *Geochemistry, Geophysics, Geosystems*, *5*(7). https://doi.org/10.1029/2003GC000681

He, M., Zhong, G., Liu, X., Liu, L., Shen, X., Wu, Z., & Huang, K. (2017). Rapid post-rift tectonic subsidence events in the Pearl River Mouth Basin, northern South China Sea margin. *Journal of Asian Earth Sciences*, *147*, 271–283. https://doi.org/10.1016/j.jseaes.2017.07.024

Horváth, F., & Cloetingh, S. A. P. L. (1996). Stress-induced late-stage subsidence anomalies in the Pannonian basin. *Tectonophysics*, *266*(1–4), 287–300. https://doi.org/10.1016/S0040-1951(96)00194-1

Hunter, J. D. (2007). Matplotlib: A 2D graphics environment. *Computing in Science and Engineering*, *9*(3), 90–95. https://doi.org/10.1109/MCSE.2007.55

Hutchison, C. S. (2004). Marginal basin evolution: The southern South China Sea. *Marine and Petroleum Geology*, *21*(9), 1129–1148. https://doi.org/10.1016/j.marpetgeo.2004.07.002

Jourdon, A., Le Pourhiet, L., Mouthereau, F., & Masini, E. (2019). Role of rift maturity on the architecture and shortening distribution in mountain belts. *Earth and Planetary Science Letters*, *512*, 89–99. https://doi.org/10.1016/j.epsl.2019.01.057

Katz, R. F., Spiegelman, M., & Langmuir, C. H. (2003). A new parameterization of hydrous mantle melting. *Geochemistry, Geophysics, Geosystems*, *4*(9), 2002GC000433. https://doi.org/10.1029/2002GC000433

Kawamoto, T., Yoshikawa, M., Kumagai, Y., Mirabueno, M. H. T., Okuno, M., & Kobayashi, T. (2013). Mantle wedge infiltrated with saline fluids from dehydration and decarbonation of subducting slab. *Proceedings of the National Academy of Sciences*, *110*(24), 9663–9668. https://doi.org/10.1073/pnas.1302040110

Keller, J. V. A., & McClay, K. R. (1995). 3D sandbox models of positive inversion. *Geological Society, London, Special Publications*, *88*(1), 137–146. https://doi.org/10.1144/GSL.SP.1995.088.01.09

Lafosse, M., Boutoux, A., Bellahsen, N., & Le Pourhiet, L. (2016). Role of tectonic burial and temperature on the inversion of inherited extensional basins during collision. *Geological Magazine*, *153*(5–6), 811–826. https://doi.org/10.1017/S0016756816000510

Li, F., Sun, Z., Ding, W., Yang, H., Xie, H., Pang, X., et al. (2021). Compression-Induced anomalous subsidence in the extensional sedimentary Basin: A numerical Study from the Pearl River mouth Basin, Northern South China Sea Margin. *Geophysical Research Letters*, *48*(18), e2021GL094750. https://doi.org/10.1029/2021GL094750

Liao, J., Zhou, D., Zhao, Z., Zhang, Y., & Xu, Z. (2011). Numerical modeling of the anomalous post-rift subsidence in the Baiyun Sag, Pearl River Mouth Basin. *Science China Earth Sciences*, *54*(8), 1156–1167. https://doi.org/10.1007/s11430-011-4184-3

Liu, H., Yumul, G. P., Dimalanta, C. B., Queaño, K., Xia, X., Peng, T., et al. (2020). Western Northern Luzon isotopic evidence of transition from proto-south China Sea to South China Sea fossil Ridge subduction. *Tectonics*, *39*(2), e2019TC005639. https://doi.org/10.1029/2019TC005639

Ma, M., Liu, C., Qi, J., Zhang, D., Zhang, S., Wang, J., & Miao, Q. (2020). Cenozoic subsidence history of the Pearl River Mouth Basin, northern South China Sea. *Geological Journal*, *55*(1), 750–770. https://doi.org/10.1002/gj.3439

Marques, F. O., & Nogueira, C. R. (2008). Normal fault inversion by orthogonal compression: Sandbox experiments with weak faults. *Journal of Structural Geology*, *30*(6), 761–766. https://doi.org/10.1016/j.jsg.2008.02.015

Oravecz, É., Balázs, A., Gerya, T., May, D. A., & Fodor, L. (2024). Competing effects of crustal shortening, thermal inheritance, and surface processes explain subsidence anomalies in inverted rift basins. *Geology*, *52*(6), 447–452. https://doi.org/10.1130/G51971.1

Pang, X., Chen, C. M., Shao, L., Wang, C., Zhu, M., He, M., et al. (2007). Baiyun movement, a great tectonic event on the Oligocene-Miocene boundary in the northern South China Sea and its implications. *Geological Review*, *53*(2), 145–151.

Perron, P., Le Pourhiet, L., Guiraud, M., Vennin, E., Moretti, I., Portier, É., et al. (2021). Control of inherited accreted lithospheric heterogeneity on the architecture and the low, long-term subsidence rate of intracratonic basins. *BSGF - Earth Sciences Bulletin*, *192*, 15. https://doi.org/10.1051/bsgf/2020038

Pinglu, L., & Chuntao, R. (1994). Tectonic characteristics and evolution history of the Pearl river mouth basin. *Tectonophysics*, *235*(1–2), 13–25. https://doi.org/10.1016/0040-1951(94)90014-0

Pinto, L., Muñoz, C., Nalpas, T., & Charrier, R. (2010). Role of sedimentation during basin inversion in analogue modelling. *Journal of Structural Geology*, *32*(4), 554–565. https://doi.org/10.1016/j.jsg.2010.03.001

Ranalli, G. (1995). *Rheology of the Earth*. Springer Science and Business Media.

Ricard, Y., & Froidevaux, C. (1986). Stretching instabilities and lithospheric boudinage. *Journal of Geophysical Research*, *91*(B8), 8314–8324. https://doi.org/10.1029/JB091iB08p08314

Rosa, M. C., Morales, N., & Assine, M. L. (2023). Transtensional tectonics during the Gondwana breakup in northeastern Brazil: Early Cretaceous paleostress inversion in the Araripe Basin. *Tectonophysics*, *846*, 229666. https://doi.org/10.1016/j.tecto.2022.229666

Franke, D., Savva, D., Pubellier, M., Steuer, S., Mouly, B., Auxietre, J. L., et al. (2014). Different expressions of rifting on the South China Sea margins. *Marine and Petroleum Geology*, *58*, 579–598. https://doi.org/10.1016/j.marpetgeo.2014.05.023

Schmalholz, S. M., & Podladchikov, Y. (1999). Buckling versus folding: Importance of viscoelasticity. *Geophysical Research Letters*, *26*(17), 2641–2644. https://doi.org/10.1029/1999GL900412

Schmidt, M. W., & Poli, S. (1998). Experimentally based water budgets for dehydrating slabs and consequences for arc magma generation. *Earth and Planetary Science Letters*, *163*(1–4), 361–379. https://doi.org/10.1016/s0012-821x(98)00142-3

Schöfisch, T., Koyi, H., & Almqvist, B. (2022). *Magnetic fabric analyses of Basin inversion: A sandbox modelling approach* (pp. 1–20). EGUsphere. https://doi.org/10.5194/egusphere-2022-1

Soret, M., Agard, P., Dubacq, B., Plunder, A., & Yamato, P. (2017). Petrological evidence for stepwise accretion of metamorphic soles during subduction infancy (Semail ophiolite, Oman and UAE). *Journal of Metamorphic Geology*, *35*(9), 1051–1080. https://doi.org/10.1111/jmg.12267

Stern, R. (2004). Subduction initiation: Spontaneous and induced. *Earth and Planetary Science Letters*, *226*(3–4), 275–292. https://doi.org/10.1016/S0012-821X(04)00498-4

Stern, R. J., & Gerya, T. (2018). Subduction initiation in nature and models: A review. *Tectonophysics*, *746*, 173–198. https://doi.org/10.1016/j.tecto.2017.10.014

Sun, Z., Lin, J., Qiu, N., Jian, Z., Wang, P., Pang, X., et al. (2019). The role of magmatism in the thinning and breakup of the South China Sea continental margin. *National Science Review*, *6*(5), 871–876. https://doi.org/10.1093/nsr/nwz116

Sun, Z., Xu, Z., Sun, L., Pang, X., Yan, C., Li, Y., et al. (2014). The mechanism of post-rift fault activities in Baiyun sag, Pearl River Mouth basin. *Journal of Asian Earth Sciences*, *89*, 76–87. https://doi.org/10.1016/j.jseaes.2014.02.018

Suo, Y., Li, S., Cao, X., Wang, X., Somerville, I., Wang, G., et al. (2020). Mesozoic-Cenozoic basin inversion and geodynamics in East China: A review. *Earth-Science Reviews*, *210*, 103357. https://doi.org/10.1016/j.earscirev.2020.103357

Tang, X., Yang, S., Zhu, J., Long, Z., Jiang, G., Huang, S., & Hu, S. (2017). Tectonic subsidence of the Zhu 1 Sub-basin in the Pearl River Mouth Basin, northern South China Sea. *Frontiers of Earth Science*, *11*(4), 729–739. https://doi.org/10.1007/s11707-016-0610-3

Turcotte, D. L., & Schubert, G. (2002). *Geodynamics*. Cambridge University Press.

Turner, J. P., & Williams, G. A. (2004). Sedimentary basin inversion and intra-plate shortening. *Earth-Science Reviews*, *65*(3–4), 277–304. https://doi.org/10.1016/j.earscirev.2003.10.002

Wang, Q., Li, S., Guo, L., Suo, Y., & Dai, L. (2017). Analogue modelling and mechanism of tectonic inversion of the Xihu Sag, East China Sea Shelf Basin. *Journal of Asian Earth Sciences*, *139*, 129–141. https://doi.org/10.1016/j.jseaes.2017.01.026

Wang, Z., Ren, J., Hu, C., & Xu, Y. (2025). Differential extrusion of Indochina-South China Block and its interplay with slab-pull tectonics: Evidence for end-Oligocene basin inversion in the Beibuwan Basin. *Tectonics*, *44*(1), e2024TC008326. https://doi.org/10.1029/2024TC008326

Wessel, P., Smith, W. H. F., Scharroo, R., Luis, J., & Wobbe, F. (2013). Generic mapping tools: Improved version released. *Eos, Transactions American Geophysical Union*, *94*(45), 409–410. https://doi.org/10.1002/2013EO450001

Wu, J., Suppe, J., Lu, R., & Kanda, R. (2016). Philippine Sea and East Asian plate tectonics since 52 Ma constrained by new subducted slab reconstruction methods: Philippine SEA PLATE tectonics-slabs. *Journal of Geophysical Research: Solid Earth*, *121*(6), 4670–4741. https://doi.org/10.1002/2016JB012923

Xie, H., Zhou, D., Shi, H., Kong, D., Li, Y., Li, F., & Cao, J. (2021). Lithospheric stretching-style variations and anomalous post-rift subsidence in the deep water sub-basins of the Pearl River Mouth Basin, northern South China Sea. *Marine and Petroleum Geology*, *131*, 105140. https://doi.org/10.1016/j.marpetgeo.2021.105140

Yang, T., Gurnis, M., & Zahirovic, S. (2016). Mantle-induced subsidence and compression in SE Asia since the early Miocene. *Geophysical Research Letters*, *43*(5), 1901–1909. https://doi.org/10.1002/2016GL068050

Yeats, R. S. (1978). Neogene acceleration of subsidence Gates in southern California.

Yumul Jr, G. P., Dimalanta, C. B., Tamayo Jr, R. A., & Maury, R. C. (2003). Collision, subduction and accretion events in the Philippines: A synthesis. *Island Arc*, *12*(2), 77–91. https://doi.org/10.1046/j.1440-1738.2003.00382.x

Zhang, J., Zhao, M., Sun, Z., Sun, L., Xu, M., Yang, H., et al. (2023). Large volume of magma involved in South China Sea rifting: Implication for mantle breakup earlier than crust. *Tectonophysics*, *853*, 229801. https://doi.org/10.1016/j.tecto.2023.229801

Zhong, X., & Li, Z. (2019). Forced subduction initiation at passive Continental margins: Velocity-driven versus stress-driven. *Geophysical Research Letters*, *46*(20), 11054–11064. https://doi.org/10.1029/2019GL084022

Zhou, F., Le Pourhiet, L., Pubellier, M., & Delescluse, M. (2025). Rifting a post-orogenic continental crust: Insights from the South China Sea. *Earth and Planetary Science Letters*, *671*, 119679. https://doi.org/10.1016/j.epsl.2025.119679

Zhou, F., Liao, J., & Le Pourhiet, L. (2023). Reactivation of pre-existing rifted basin by forced subduction initiation in the South China Sea. *Zenodo*. [Dataset]. https://doi.org/10.5281/zenodo.17567265

Zhou, X., Li, Z.-H., Gerya, T. V., Stern, R. J., Xu, Z., & Zhang, J. (2018). Subduction initiation dynamics along a transform fault control trench curvature and ophiolite ages. *Geology*, *46*(7), 607–610. https://doi.org/10.1130/G40154.1

Ziegler, P. A. (1987). Late Cretaceous and Cenozoic intra-plate compressional deformations in the Alpine foreland—a geodynamic model. *Tectonophysics*, *137*(1–4), 389–420. https://doi.org/10.1016/0040-1951(87)90330-1